Surface & Coatings Technology 224 (2013) 120–125

Contents lists available at SciVerse ScienceDirect

Surface & Coatings Technology

journal homepage: www.elsevier.com/locate/surfcoat

Microstructure, residual stress, and fracture of sputtered TiN films

Liqiang Zhang [a], Huisheng Yang [a], Xiaolu Pang [a,*], Kewei Gao [a], Alex A. Volinsky [b]

[a] Department of Materials Physics and Chemistry, University of Science and Technology Beijing, Beijing 100083, China
[b] Department of Mechanical Engineering, University of South Florida, Tampa, FL 33620, USA

ARTICLE INFO

Article history:
Received 26 October 2012
Accepted in revised form 6 March 2013
Available online 21 March 2013

Keywords:
TiN films
Residual stress
Hardness
Fracture toughness

ABSTRACT

Morphology, structure, residual stress, hardness, and fracture toughness of magnetron sputtered titanium nitride (TiN) thin films, deposited at 300 °C with a thickness in the 0.3- to 2-μm range, were characterized. Film microstructure, the origin of residual stress, and its effect on the fracture toughness and hardness were analyzed. The grain size increased with the film thickness, with 1- to 2-μm-thick films having high pore density. For the 2-μm film, subgrains appeared at grain boundaries. X-ray diffraction showed (200) to (111) preferred orientation transition. The stress in the TiN films changed from highly compressive (−1.1 GPa) to tensile with the film thickness, reaching 0.68 GPa. Larger grain size, initial porosity, and subgrain generation are reasons for significant changes in the residual stress. Average hardness measured by nanoindentation is 23.2 ± 0.6 GPa. The hardness of the films in compression is higher than in tension. Hardness variation with the film thickness is mainly due to the grain size and microstructure effects. The fracture toughness decreases with the film thickness, depending on the stress state and value. Compressive stress can significantly improve TiN film fracture toughness, while tensile stress seriously degrades it.

© 2013 Elsevier B.V. All rights reserved.

1. Introduction

Thin TiN films deposited by physical vapor deposition have a wide range of applications in machine components, industrial tools, computer disc drives, precision instruments, and human replacement organs [1–3]. TiN has high hardness and good chemical and metallurgical stability [4]. However, such films, when grown on rigid substrates, are generally in a stressed state, which influences the film's mechanical performance [5]. Stress film thickness dependence for TiN films was reported, attributed to lower defect density in thicker films [6]. Janssen [5] observed a highly compressive average residual stress for thinner TiN films, which decreased for thicker films, and proved that the actual stress in PVD TiN films is a gradient over the thickness and that the stress was not relaxed in thicker films. However, in the study of Köstenbauer et al. [6], it was not observed that the stress in the TiN films undergoes a change from highly compressive to tensile with increasing thickness. Daniel et al. [7] and Janssen [8] reported that sputtered Cr/CrN dual films' stress state is strongly affected by the Cr bonding layer, including its thickness and structure. In the experiment of Daniel et al. [7], the effect of the ion irradiation on the development of the compressive stress was dependent on grain size, texture, and morphology and can be controlled by the growth conditions. Similarly, the tensile thermal stress varies with the layer thickness because the thermal expansion coefficient is a structure-dependent property, varying with grain size. On the basis of these results, the average stress, as a sum of basic competing structure-dependent stress components, determines the final stress level in the layer. However, Janssen [8] showed that the stress in Cr/CrN is not uniform over the thickness of the film. High tensile stresses are observed near the substrate–film interface. Lower tensile stresses are observed further away from the interface. Moreover, it has been shown that the tensile stress is generated at the grain boundaries. When the film deposition is accompanied by an ion bombardment, compressive stress is generated. The tensile and compressive stresses in these films are independent and additive, but the results did not hold for all high melting point films, notably not for TiN. In this paper, the stress transition from compression to tension is discussed, along with the corresponding mechanism and its effects on the mechanical properties, including hardness and fracture toughness.

2. Experimental details

TiN films were grown by reactive RF-pulsed magnetron sputter deposition in an industrial PVD system at 300 °C. Single crystal silicon substrates (110 crystal orientation, 335 μm thick) were moved in front of a 76-mm diameter titanium target. Nitrogen and argon flow during deposition was 1.4 and 15 standard-state cubic centimeter per minute, respectively. The base pressure in the sputtering chamber was below 4.8×10^{-3} Pa, whereas the deposition pressure was kept at 0.3 Pa. The Ar pressure was 0.25 Pa. The growing film was ion bombarded by applying a substrate bias voltage of −80 V; the target power was 300 W, resulting in a deposition rate of 7.6 nm/min.

Before sputtering, substrates were cleaned in acetone and ethanol for 10 min, respectively, and subjected to 10 min in situ Ar plasma cleaning at 50 W RF power to remove any contaminants on the substrate surface

* Corresponding author. Tel./fax: +86 10 82376048.
E-mail address: pangxl@mater.ustb.edu.cn (X. Pang).

0257-8972/$ – see front matter © 2013 Elsevier B.V. All rights reserved.
http://dx.doi.org/10.1016/j.surfcoat.2013.03.009

and to activate the surface. The target was cleaned using argon (99.99% pure) gas discharge plasma for 10 min. Initially, an adhesion layer of Ti metal was deposited for 10 min, followed by TiN deposition. Film thickness was controlled by adjusting the deposition time and ranged from 285 to 2365 nm.

The films were characterized using field emission scanning electron microscopy (FSEM, 10 kV) and X-ray diffraction (DMAX-RB 12 kW) with Cu Kα radiation, and a scan speed of 2°/min was employed in the 30° to 60° 2θ range. The film stress was calculated from the substrate curvature radius change using the Stoney equation [9]. The substrate profile was measured with Veeco Dektak 150 stylus profilometer. Hardness (H) and elastic modulus (E) were measured using nanoindentation techniques. Finally, the fracture toughness was evaluated by measuring the radial cracks. Radial cracks were introduced at the surface of TiN films when indented with a sharp Vickers indenter tip.

3. Results and discussion

3.1. Film structure

FSEM micrographs in Fig. 1 show surface microstructure of TiN films with different thickness. The morphology of the TiN films changes significantly with the film thickness. For the 286-nm-thick film, the grain size is very small (Fig. 1a), gradually increasing with the film thickness. For the 2366-nm-thick film, subgrains appear at grain boundaries, and structure becomes denser, compared with thinner films (Fig. 1d). TiN films morphology changed significantly with increasing thickness, which also affects the residual stress.

X-ray diffraction (XRD) $\theta/2\theta$ scans from reactively magnetron-sputtered TiN layers deposited with increasing thickness on Si (110) substrates are presented in Fig. 2. The diffraction patterns reveal the presence of the fcc monophase B1–NaCl structure, showing mainly (111) and (200) reflections. Texture transitions from (200) to (111) preferred orientation with increasing film thickness. Above 516 nm, films show (111) preferred orientation. The big shift of the peak position to higher 2θ diffraction angles, with respect to the relaxed structure of randomly oriented fcc TiN in thinner films, indicates in-plane compression in the layers. This result is consistent with the measured residual stress in the films. Fig. 3 shows the values of the full width at half maximum (FWHM) of the rocking curve around the (111) diffraction peak. FWHM (B) initially decreased with the film thickness and then increased due to the subgrains generation at grain boundaries (Fig. 1d). As seen in Fig. 3, the FWHM (B) of the 1928-nm film is the narrowest, revealing the best crystalline structure.

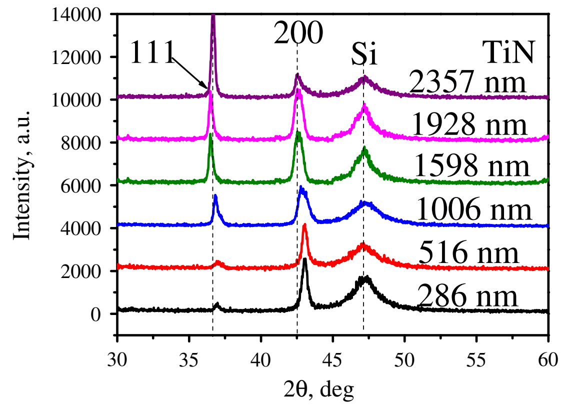

Fig. 2. XRD spectra of different thickness TiN films.

The size of the <D> in the films was calculated as [10]

$$\langle D\rangle = \frac{0.9\lambda}{B\cos\theta} \tag{1}$$

Here, λ is the XRD wavelength, θ is the Bragg's angle. Parameter $\langle D\rangle$ corresponds to the average length of crystalline domains in the direction of the diffraction vector and represents crystalline regions with no planar defects [11], whereas B is the FWHM value. Fig. 3 indicates that $\langle D\rangle$ initially increased with the film thickness in the 286- to 1928-nm range and then decreased for the 2366-nm film. The reason may be due to the subgrains created at grain boundaries. The subgrains can be clearly seen in Fig. 1d. This result, thus, agrees with the FSEM surface micrographs (Figs. 2 and 4).

The FSEM cross-sectional view in Fig. 4 illustrates a structure of the 1598-nm-thick Ti/TiN film grown on Si (110). An adhesion layer of Ti is clearly visible. Although the film near the substrate consists of very

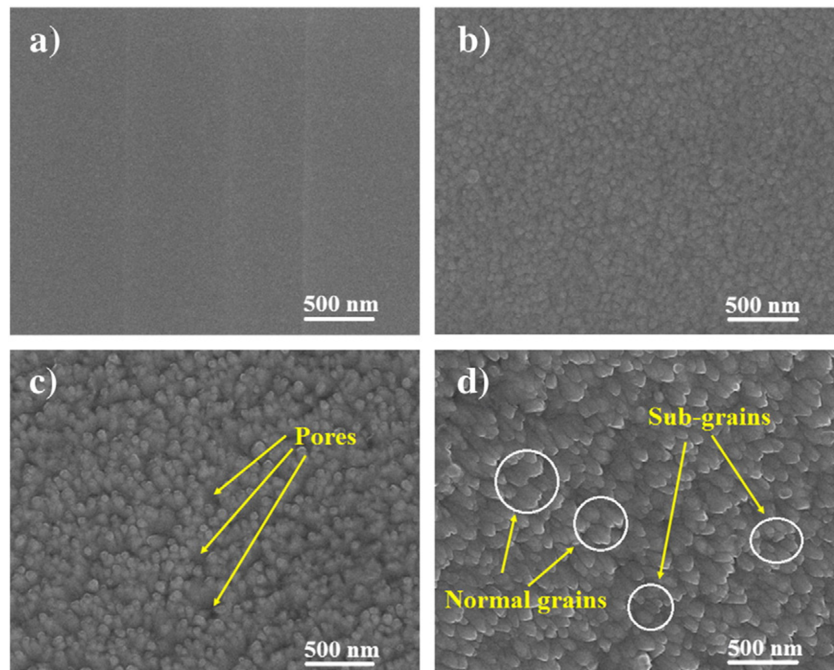

Fig. 1. FSEM micrographs showing the surface morphology of (a) 286 nm, (b) 1006 nm, (c) 1928 nm, and (d) 2366 nm TiN films. (EHT = 10 kV; WD = 9.1 mm).

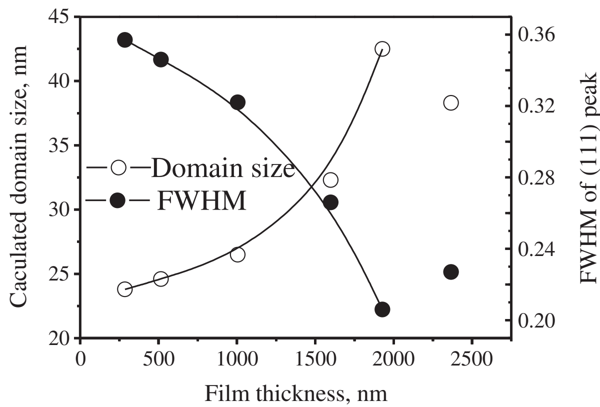

Fig. 3. FWHM of TiN films (111) reflections. Trend lines added for clarity.

fine crystalline grains, larger columnar grains with almost parallel vertical boundaries developed further from this transition zone to the top of the film. Besides competitive growth phenomena, the reason for these structural features is oxygen contamination of the grain boundaries, resulting in limited coalescence at the very early growth stage [12]. Oxygen content in all layers is typically below 1 at.%, measured by WDX [7].

3.2. Residual stress in TiN films

The residual stress in the films, σ, was calculated using the Stoney equation [9]:

$$\sigma = \frac{1}{6}\left(\frac{1}{R_a} - \frac{1}{R_b}\right)\frac{E}{1-\nu}\frac{t_s^2}{t_f} \quad (2)$$

Here, R_b and R_a are radii of the substrate curvature before and after film deposition, respectively, E is the Young's modulus, ν is the Poisson's ratio of the substrate, and t_s and t_f are the thicknesses of the substrate and the film, respectively. Substrate profiles were measured using Dektak 150 stylus profilometer. Profiles corresponding to compressive and tensile stresses in the film are shown in Fig. 5.

In Fig. 6a, the average residual stress is plotted as a function of the film thickness. For the 286-nm film, −0.85 GPa compressive stress was calculated, gradually increasing to −1.1 GPa for the 516-nm-thick film. Subsequently, compressive stress changes to tensile at 1006-nm film thickness and increases further, reaching 0.68 GPa for the 1928-nm-thick film. The residual stress trend observed in this paper is different from those of

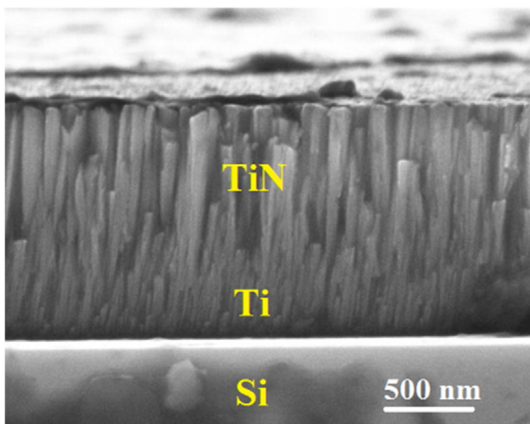

Fig. 4. FSEM image of the 1598-nm-thick TiN film cross-sectional microstructure (EHT = 10 kV; WD = 9.4 mm).

Machunze et al. [5] and Köstenbauer et al. [6]. This is likely caused by the adhesive layer and the deposition temperature.

As seen in Fig. 6a, the stress in sputtered TiN films can be either compressive or tensile, depending on the film thickness. The transition from compressive to tensile stress can be explained by the following two reasons [13,14]. First, as the size of crystals increases, the number of defects decreases, and films become dense, causing a natural tendency of the film to develop tensile stress with the film thickness. Second, compressive stresses develops in the film by "atomic shot peening," associated with the collision of neutral inert gas atoms (created in the sputtering process) with the growing film.

Compressive stresses can be understood qualitatively in terms of both the implantation of atoms in the film during deposition and the microplastic deformation, associated with the atomic collisions. Energetic argon atoms become implanted into the film, resulting in compressive stresses. The excess atoms dilate the material near the surface, which leads to compressive stresses due to the constraint of the underlying film. Also, atomic collisions with the growing surface result in plastic deformation events. Each surface element can be deformed plastically. This deformation would occur by incremental dislocations movement in the film or other shear processes. Again, the constraint of the underlying film leads to biaxial compression in the film. The tensile stresses present in sputtered film depend on the tendency of the film to shrink once attached to the substrate. Thus, the stresses that develop are associated with the internal atomic rearrangement or densification of the film. If the sputtered structure relaxes to a denser state, then intrinsic tensile stresses develop in the film.

At the initial deposition stage, the grain size is very small in the 286- to 516-nm film thickness range. Compressive stress originates from the coating structure with dense point defects. At this stage, attachment to the substrate restrains lattice expansion, significantly contributing to residual compressive stress. Along with increasing film thickness (controlled by sputtering time), grain size increases and the density of grain boundaries (length per surface area) decreases, which results in

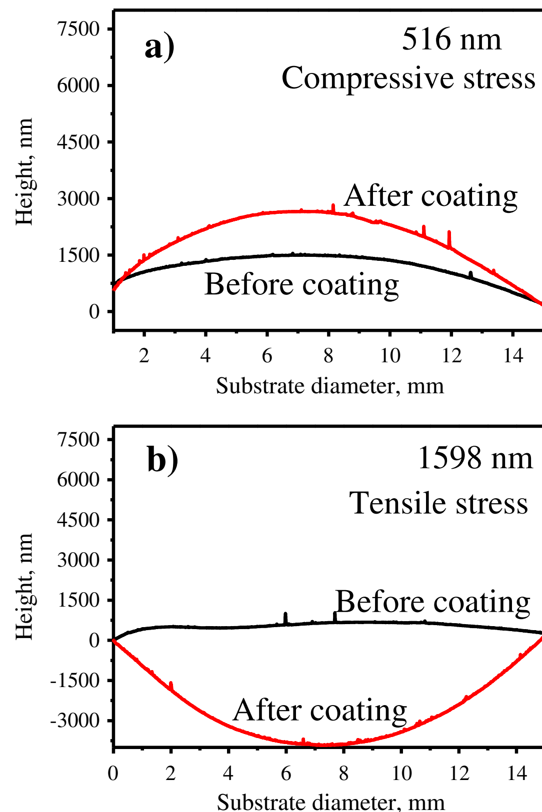

Fig. 5. Surface profiles of TiN films: (a) 516 nm in compression; (b) 1598 nm in tension.

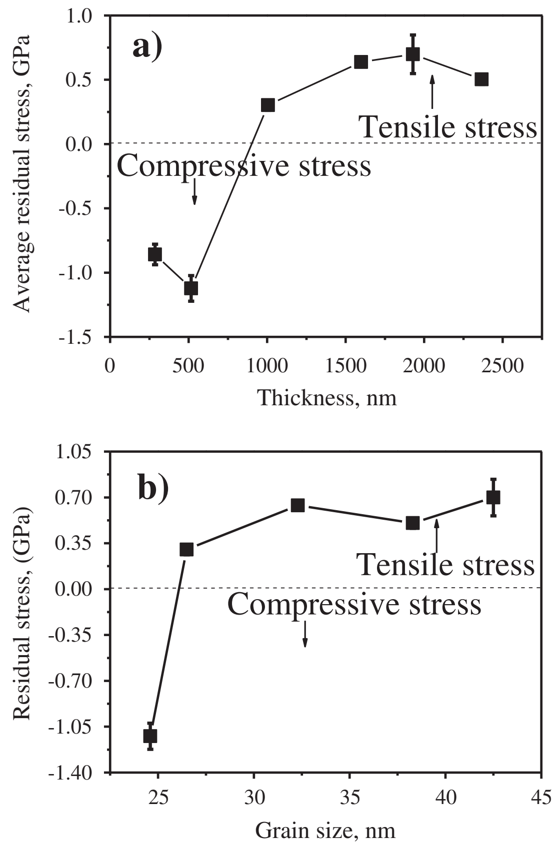

Fig. 6. (a) Average residual stress in TiN films as a function of film thickness. (b) Average residual stress in TiN film as function of grain size.

reduced porosity in the films. The lower the grain boundaries density, the less possibility exists for the extra atoms to be inserted into the grain boundaries [15], which, in turn, decreases the compressive stress, transforming into tensile stress. Chaudhart [15] pointed out that grain boundaries are less dense than the crystal lattice, so that grain growth (elimination of some grain boundaries) leads to densification of the film and thus to tensile stresses in the film. Additionally, for the 2366-nm-thick film, with a dense structure, the pores almost disappeared, and subgrains were generated at grain boundaries (Fig. 1d). It also indicates that the generation of subgrains and grains coarsening in TiN coatings results in stress relaxation due to defects annihilation. Similar findings have been reported by Köstenbauer et. al. [11], where films were thermally cycled to elevate the residual stress. It was indicated that temperature gives rise to stress relaxation due to defects annihilation (often referred to as recovery) and grain coarsening in nitride coatings.

In the study of Chang et al. [16], it was indicated that the increase in the residual stress of the TiN film is caused by the smaller grain size and the transition of the texture from (200) to (111) preferred orientation. This conclusion agrees well with our findings. The relationship between grain size and residual stress was also investigated. In this paper, the grain size is equivalent to the size of the coherently diffracting domains $\langle D \rangle$. The result is shown in Fig. 6b. It indicates that TiN films with grain size smaller than 25 nm exhibit higher compressive stress, and above 25 nm have low tensile stress. Reference [16] also indicates that grain growth generally leads to stress relaxation when the film is under compressive stress. When the initial grain size is below a critical value, grain growth can occur by normal boundary migration and generates tensile stress in the plane of the film. This result agrees well with our investigation.

3.3. Hardness and elastic modulus measurements

Hardness, H, and elastic modulus, E, are two important thin film mechanical properties that can be measured using nanoindentation techniques. In this experiment, the nanoindentation loading rate was 10 nm/s and the values of hardness and elastic modulus were the average values from loading displacement between 1/7 and 1/10 of the TiN films thickness. Table 1 shows H and E variations of the TiN film deposited on Si (110) versus thickness. An average value of the hardness of 23.2 ± 0.6 GPa was obtained by nanoindentation in the 300- to 1500-nm depth range. For the 2366-nm-thick film, a 16.87-GPa hardness was measured. It also indicates that E increases from 264 to 350 GPa rapidly with the film thickness (286–1928 nm) and subsequently decreases rapidly to 286 GPa.

The study of Hakamada et al. [17] shows that the hardness increases with decreasing grain size, which is consistent with the present observation. The relationship between the hardness and the grain size was established [18–20]:

$$H = H_0 + kd^n \tag{3}$$

Here, H is the hardness, d is the average grain size, n is the grain size exponent (typically −1/2), and H_0 and k are constants. Fig. 7 shows the average hardness plotted as a function of the reciprocal square root of the average grain diameter for different thickness coatings. It suggests that the coatings in the 516- to 1928-nm thickness range follow the modified Hall–Petch relationship [21]. For the 2366-nm-thick film, deviation from the linear relationship is most likely caused by the subgrains generation.

Comparing residual stress with the hardness of different thickness films (Fig. 8), one can see that the hardness of the film in compression is higher than that in tension. The variation of the hardness with increasing thickness mainly depends of the grain size and microstructure. Two possible reasons for the decreasing elastic modulus with decreasing film thickness could be suggested [22]. A few nanometer thick interfacial reaction layers formed at the initial deposition stage, and a second reason would be the inhomogeneous film structure during the early growth stages.

The mechanical behavior of hard coatings is well characterized, not only by their hardness, H, but also by their effective Young's modulus $E^* = E/(1-\nu^2)$ and elastic recovery. Moreover, measured H and E values permit simple calculation of the H^3/E^{*2} ratio, which provides information about the material resistance to plastic deformation [23]. The higher it is, the higher the H^3/E^{*2} ratio is. The likelihood of plastic deformation is therefore significantly reduced in materials with high H and low E. The H^3/E^{*2} ratio is plotted in Fig. 9. It indicates that the resistance of the film to plastic deformation decreases with the film thickness. The resistance of the 2366-nm-thick film to plastic deformation is a little better than that of the 1928-nm-thick film. This results from the subgrains generation in the 2366-nm-thick film.

3.4. Film fracture toughness

Toughness is one of the most important mechanical properties. The term toughness refers to the ability of a material to absorb energy

Table 1
TiN films hardness and elastic modulus.

Film Thickness, nm	Hardness (Error Bars), GPa	Elastic Modulus (Error Bars), GPa
286	23.26 (0.85)	263.6 (5.7)
516	23.88 (0.71)	268.52 (2.6)
1006	22.69 (0.91)	282.51 (3.11)
1598	23.06 (0.33)	316.3 (2.9)
1928	19.08 (1.3)	350.4 (18.1)
2366	16.87 (0.87)	285.98 (10.3)

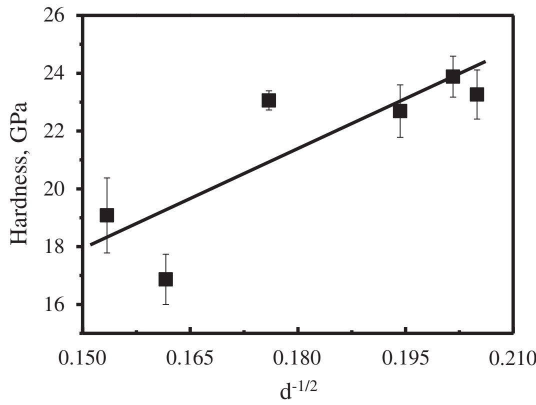

Fig. 7. Hardness as a function of the reciprocal square root of the grain size ($d^{-1/2}$).

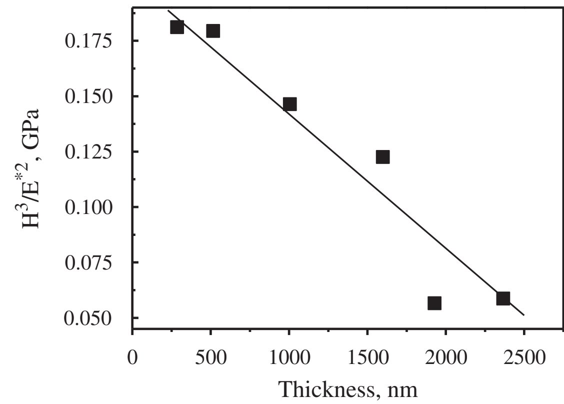

Fig. 9. Variation of the H^3/E^{*2} ratio with TiN film thickness.

during deformation, up to fracture, usually measured in terms of fracture toughness [10]. A radial crack was introduced at the surface of a ceramic film when indented with a sharp Vickers indenter tip (Fig. 10a). The relationship between the fracture toughness and the length of radial cracks was established [24]:

$$K_{IC} = \alpha \left(\frac{E}{H}\right)^{1/2} \frac{P}{c^{3/2}} \tag{4}$$

Here, P is the peak load at indentation, c is the crack length, and α is the empirical constant, which depends on the geometry of the indenter ($\alpha = 0.016$ for the Vickers indenter). It is required that $c \geq 2a$ (a is the radius of the impression; Fig. 10a). E and H were measured using nanoindentation. Table 2 shows different radial crack lengths of TiN films indented by Vickers indenter tip with 1.96 N normal load. The micrograph of radial cracks in a 1928-nm-thick TiN film is shown in Fig. 10b.

The fracture toughness, K_{IC}, was calculated using Eq. (4). The results are also summarized in Table 2, indicating that initially K_{IC} increases with the film thickness (286- to 516-nm range) and then rapidly decreases (>1006 nm). For the 1928-nm-thick film, K_{IC} of 0.68 MPa · $m^{1/2}$ was measured, which is the lowest value among all coatings.

Fig. 11 shows TiN films fracture toughness variation as functions of the H^3/E^{*2} ratio and the residual stress. It indicates that the fracture toughness, K_{IC}, increases with the increasing resistance to plastic deformation. However, for the 2366-nm-thick film, the H^3/E^{*2} ratio is low whereas the fracture toughness, K_{IC}, is high. This may be caused by the subgrains generation. The generation of subgrains results in a denser structure and thus improves the fracture toughness.

The relationship between residual stress and fracture toughness is also seen in Fig. 11b. It indicates that compressive stress effectively improves fracture toughness. The higher compressive stress value is, the higher is the fracture toughness, K_{IC}. However, tensile stress can significantly degrade film fracture toughness. In Fig. 11b, the fracture toughness decreases rapidly with increasing tensile stress. The crack initiation and growth is driven by tensile stress; however, the residual compressive stress at the crack tip can close the crack. When crack propagates, the tensile stress driving the crack initiation and growth must overcome the compressive stress in the film, consuming additional energy.

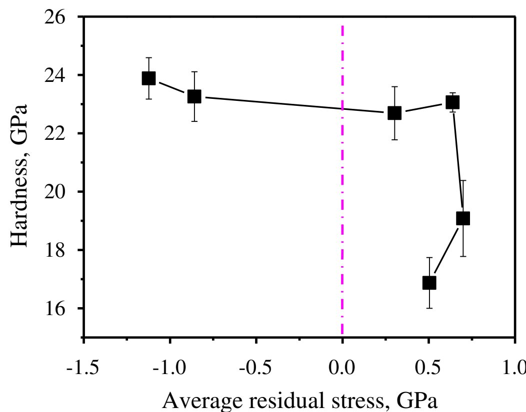

Fig. 8. Film hardness as a function of residual stress.

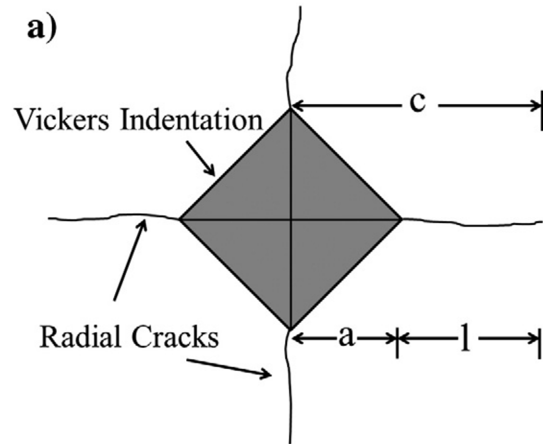

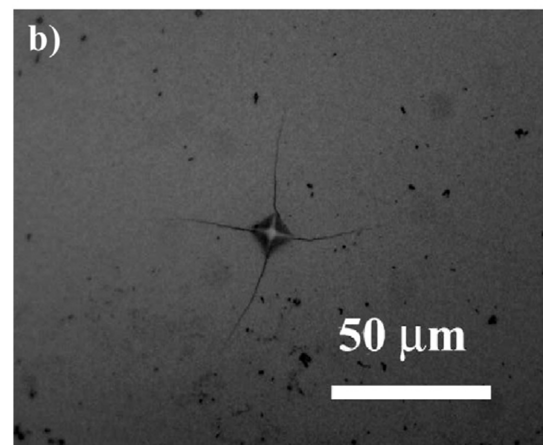

Fig. 10. (a) Schematic illustration of radial cracking upon Vickers indentation and (b) 1.96 N load Vickers indentation radial cracks in the 1928-nm-thick TiN film.

Table 2
Crack length and fracture toughness, K_{IC}.

Film thickness, nm	Crack length, μm	K_{IC}, MPa · $m^{1/2}$
286	18.3	1.35
516	16.8	1.56
1006	18.3	1.41
1598	22.3	1.10
1928	34	0.68
2366	21.7	1.28

Therefore, the resistance to crack propagation increases and the fracture toughness is improved. To the contrary, tensile stress tends to aid the crack propagation, thus the fracture toughness in tension is lower.

4. Conclusions

In this work, film structure, the origin of residual stress, and the effect of residual stress on the fracture toughness and hardness were studied in sputtered TiN films of different thickness. Grain size increases with the film thickness, while 1- to 2-μm-thick films are porous. For the 2366-nm-thick film, subgrains appear at grain boundaries, and structure gets denser. The subgrains generated at grain boundaries significantly affect mechanical properties and texture. The stress in the TiN films undergoes a change from highly compressive (−1.1 GPa) to tensile with increasing thickness and tends to increase further, reaching 0.68 GPa. The development of compressive stress in the film at the initial stage by "atomic shot peening" is associated with the collision of neutral inert gas atoms (created in the sputtering process) with the growing film. However, tensile stresses developed in sputtered films at a later stage and depend on the tendency of the film to shrink once it is attached to the substrate and cooled to room temperature. The hardness of the films in compression is higher than in tension. Hardness variation with the film thickness is mainly affected by the grain size and microstructure. The fracture toughness decreases with thickness and strongly depends on the residual stress. Compressive stress can effectively improve the film fracture toughness, whereas tensile stress dramatically degrades it. In tension, the higher the stress is, the lower is the fracture toughness.

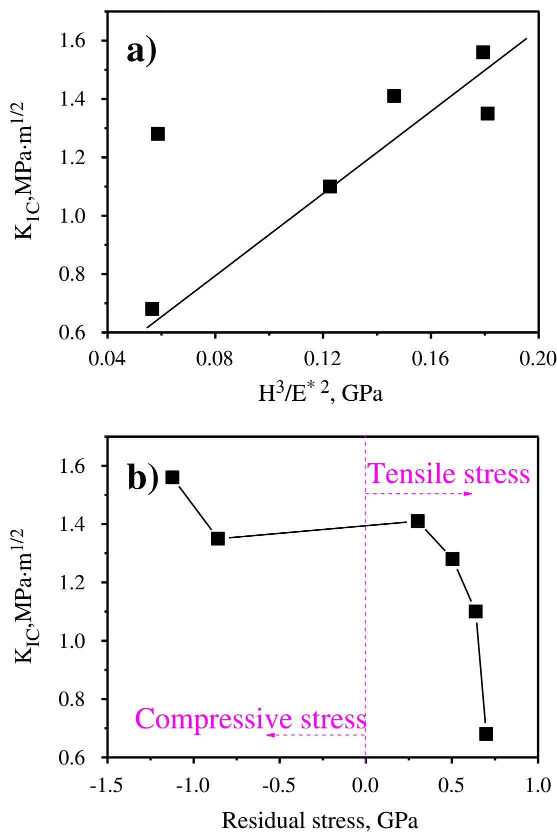

Fig. 11. TiN films fracture toughness as functions of (a) H^3/E^{*2} and (b) residual stress.

Acknowledgments

This work was supported by the National Nature Science Foundation of China (grant nos. 51001013 and 51271022), the Fok Ying Tung Education Foundation (grant no. 132001), and the Fundamental Research Funds for the Central Universities.

References

[1] K. Holmberg, H. Ronkainen, K. Holmberg, A. Laukkanenl, Wear 254 (2003) 278.
[2] X. Pang, H. Yang, K.W. Gao, Y. Wang, A.A. Volinsky, Thin Solid Films 519 (2011) 5353.
[3] R. Machunze, G.C.A.M. Janssen, Thin Solid Films 517 (2009) 5888.
[4] F.J. Espinoza-Beltrán, O. Che-Soberanis, L. García-González, J. Morales-Hernández, Thin Solid Films 437 (2003) 170.
[5] R. Machunze, G.C.A.M. Janssen, Surf. Coat. Technol. 203 (2008) 550.
[6] H. Köstenbauer, G.A. Fontalvo, M. Kapp, J. Keckes, C. Mitterer, Surf. Coat. Technol. 201 (2007) 4777.
[7] R. Daniel, K.J. Martinschitz, J. Keckes, C. Mitterer, Acta Mater. 58 (2010) 2621.
[8] G.C.A.M. Janssen, Thin Solid Films 515 (2007) 6654.
[9] G.C.A.M. Janssen, M.M. Abdalla, F. van Keulen, B.R. Pujada, B. van Venrooy, Thin Solid Films 517 (2009) 1858.
[10] K. Kusaka, T. Ao, T. Hanabusa, K. Tominaga, Thin Solid Films 332 (1998) 247.
[11] H. Köstenbauer, G.A. Fontalvo, J. Keckes, C. Mitterer, Thin Solid Films 516 (2008) 1920.
[12] M. Adamik, P.B. Barna, Surf. Coat. Technol. 80 (1996) 109.
[13] J. Xiong, W. Qin, X. Cui, B. Tao, J. Tang, Y. Li, Physica C 455 (2007) 52.
[14] P.R. Guduru, E. Chason, L.B. Freund, J. Mech, Phys. Solids 51 (2003) 2127.
[15] P. Chaudhart, J. Vac. Sci. Technol. 9 (1972) 520.
[16] C.-L. Chang, J.-Y. Jao, W.-Y. Ho, D.-Y. Wang, Surf. Coat. Technol. 201 (2007) 6702.
[17] M. Hakamada, Y. Nakamoto, H. Matsumoto, H. Iwasaki, Y. Chen, H. Kusuda, M. Mabuchi, Mater. Sci. Eng., A 457 (2007) 120.
[18] R.W. Siegel, G.E. Fougere, Mater. Res. Soc. Symp. Proc. 362 (1995) 219.
[19] H. Chang, C.J. Altstetter, R.S. Averback, J. Mater. Res. 7 (1992) 2962.
[20] D.E. Wolfe, J. Singh, K. Narasimhan, Surf. Coat. Technol. 165 (2003) 8.
[21] J.W. Wang, W.Z. Li, H.D. Li, B. Shi, J.B. Luo, Thin Solid Films 366 (2000) 117.
[22] J.W. Wang, C.S. Lee, D.H. Ko, J.H. Ham, K.Y. Eun, K.R. Lee, Diamond Relat. Mater. 10 (2001) 2069.
[23] J. Musil, F. Kunc, H. Polakova, Surf. Coat. Technol. 154 (2002) 304.
[24] S. Zhang, X. Zhang, Thin Solid Films 520 (2012) 2375.